Terahertz chiral photonic-crystal cavities with broken time-reversal symmetry

Fuyang Tay[1,2], Stephen Sanders[1], Andrey Baydin[1,3], Zhigang Song[4], Davis M. Welakuh[5], Alessandro Alabastri[1,3], Vasil Rokaj[6,7,8], Ceren B. Dag[6,7], Junichiro Kono[1,3,9,10*]

[1*]Department of Electrical and Computer Engineering, Rice University, Houston, 77005, Texas, USA.
[2]Applied Physics Graduate Program, Smalley–Curl Institute, Rice University, Houston, 77005, Texas, USA.
[3]Smalley–Curl Institute, Rice University, Houston, 77005, Texas, USA.
[4]John A. Paulson School of Engineering and Applied Sciences, Harvard University, Cambridge, 02139, Massachusetts, USA.
[5]Max Planck Institute for the Structure and Dynamics of Matter, Luruper Chaussee 149 Hamburg, 22761, Germany.
[6]ITAMP, Harvard-Smithsonian Center for Astrophysics, Cambridge, 02138, Massachusetts, USA.
[7]Department of Physics, Harvard University, Cambridge, 02138, Massachusetts, USA.
[8]Department of Physics, Villanova University, Villanova, 19085, Pennsylvania, USA.
[9]Department of Physics and Astronomy, Rice University, Houston, 77005, Texas, USA.
[10]Department of Materials Science and NanoEngineering, Rice University, Houston, 77005, Texas, USA.

*Corresponding author(s). E-mail(s): kono@rice.edu;

Abstract

Strong coupling between matter and vacuum electromagnetic fields in a cavity can induce novel quantum phases in thermal equilibrium via symmetry breaking. Particularly, coupling with circularly polarized fields can break time-reversal symmetry, leading to topological modifications in the band structure. Therefore, chiral optical cavities that

host chiral vacuum fields are being sought, especially in the terahertz (THz) frequency range, where various large-oscillator-strength resonances exist. Here, we present a novel approach to achieving THz chiral photonic-crystal cavities (PCCs) with high-quality factors ($>$400) using a magnetoplasma in a lightly doped semiconductor. Numerical simulations of an optimized structure based on InSb in a small perpendicular magnetic field ($\sim$0.2 T) show chiral cavity resonances with near-perfect ellipticity at the surfaces of the central dielectric layer, where one can place atomically thin materials like monolayer graphene. We theoretically estimate an energy gap on the order of **1** meV in graphene when coupled to our proposed chiral cavity, which is potentially measurable in experiments. These THz chiral PCCs offer a promising platform for exploring new phases in cavity-dressed condensed matter with broken time-reversal symmetry.

Keywords: cavity material engineering, chiral cavities

Introduction

The strong coupling of condensed matter with radiation inside a photonic cavity has recently attracted considerable attention due to the possibility that unusual new quantum phases may arise in thermal equilibrium without an external driving field. Namely, a certain matter resonance can be strongly coupled, or dressed, by vacuum electromagnetic fields, or virtual photons, that surround the matter in the cavity [1–4]. Recent experiments on condensed matter in cavities have revealed new effects such as the breakdown of the topological protection of the quantum Hall effect [5, 6] and thermal control of the metal-to-insulator transition in a charge-density-wave system [7]. One approach toward the creation of a new ground state in a material is by breaking a specific material symmetry with light. For example, circularly polarized light with finite angular momentum can break time-reversal symmetry (TRS), resulting in a gap opening and the formation of topological Floquet bands in graphene [8]. Recent theoretical studies suggest that coupling a material with a circularly polarized vacuum field inside a chiral cavity can achieve band structure engineering similar to Floquet physics [1, 9, 10]. Therefore, a robust chiral cavity design that can be used to break TRS in a material is desired.

Chiral matter exhibits different optical responses to left circularly polarized (LCP) and right circularly polarized (RCP) light. Chirality can be induced by breaking either mirror symmetry (e.g., spiral structures) or TRS (e.g., adding an external magnetic field). The nature of standing waves formed in a chiral object depends on the type of symmetry that is broken. In chiral systems that lack mirror symmetry, their optical responses to circularly polarized light are reciprocal since TRS remains preserved. Specifically, the responses to LCP and RCP light do not change when the direction of propagation is reversed [11]. For example, consider a chiral slab that only allows the propagation of RCP light in both directions. In this case, RCP light propagating in opposite directions forms a helical standing wave inside the slab, as illustrated in Fig. 1a. The polarization of the helical standing wave rotates along the z direction, while the amplitude varies sinusoidally with time (t), given by $\mathbf{E}_{\text{standing}} \propto \cos(\omega t)[\mathbf{e}_x \cos(kz) \pm \mathbf{e}_y \sin(kz)]$ [12, 13], where k is the wave vector in the z direction and ω is the frequency. Note that the electric field of this standing wave remains linearly polarized at a given z. By contrast, a chiral system is nonreciprocal if TRS is broken. The roles of LCP and RCP light are interchanged when the direction of propagation is reversed

while the magnetic field direction remains unchanged. For example, consider a chiral slab that only allows the forward propagation of RCP light and the backward propagation of LCP light. In this slab, the standing wave becomes a static cosine wave along the z direction, with its polarization rotating with t, as depicted in Fig. 1b. This wave can be described by $\mathbf{E}_{\text{standing}} \propto \cos(kz)[\mathbf{e}_x \sin(\omega t) \pm \mathbf{e}_y \cos(\omega t)]$ [12, 13]. The electric field of this standing wave is circularly polarized at any z.

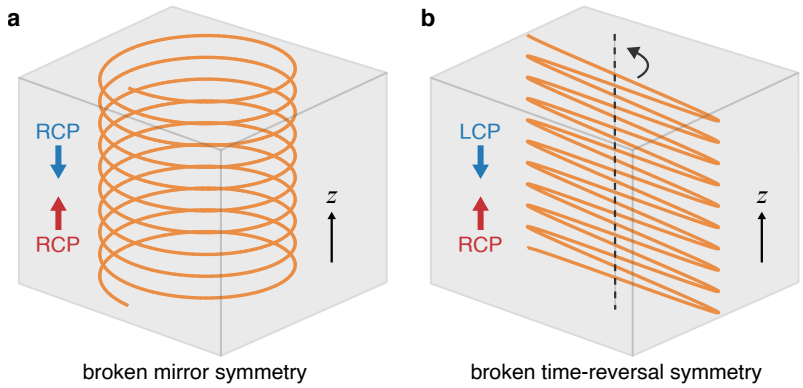

Fig. 1 Standing waves in a chiral slab with two types of chirality – broken mirror symmetry versus broken time-reversal symmetry. a–b, Chiral standing waves (orange trace) occur when circularly polarized light propagates in opposite directions along the z axis (red and blue arrows) with (**a**) the same handedness and (**b**) the opposite handedness inside the chiral material (gray slab). The standing wave with broken mirror symmetry in (**a**) is helical along the z axis, while its amplitude varies sinusoidally with time. By contrast, the standing wave with broken time-reversal symmetry in (**b**) is sinusoidal along the z axis, while its polarization rotates constantly with time. Only in the case of (**b**), the electric field is circularly polarized at any z.

Past studies have focused on chiral artificial materials that only break mirror symmetry, including photonic crystals [14–18] and metamaterials and plasmonic nanostructures [12, 19–22], by using specific geometrical designs. In recent years, there have been discussion and realization of chiral cavities with broken TRS. First, a chiral cavity consisting of two Faraday mirrors, which combine a Faraday rotator and a regular mirror, has been proposed [1, 13]. The Faraday rotator induces a phase difference between chiral standing waves with opposite handedness, causing the nodes and antinodes of the standing waves to be located at different positions inside the cavity. However, this design has yet to be demonstrated experimentally. More recently, chiral cavities with broken TRS have been demonstrated based on different mechanisms [23–25]. Suárez-Forero *et al.* have realized a chiral cavity consisting of two $MoSe_2$ mirrors that exhibit spin-selective reflection in a high magnetic field [23]. The Fabry–Pérot modes in the visible range were made nondegenerate between LCP and RCP by the applied magnetic field. Andberger *et al.* and Aupiais *et al.* have developed chiral plasmonic cavities that operate in the terahertz (THz) frequency range by coupling plasmonic resonators with the cyclotron resonance of a two-dimensional electron gas in GaAs [24] or a magneto-plasma in bulk InSb [25]. The quality (Q) factor of the fabricated cavity remained low, and the degree of chirality, or ellipticity, was not perfect and spatially uniform.

Here, we describe a novel scheme for designing a THz chiral photonic-crystal cavity (PCC) with broken TRS by using a magnetoplasma in lightly doped InSb in a small applied magnetic field. We utilize the nonreciprocal nature of THz transmission through the magnetoplasma in InSb due to free-carrier cyclotron resonance to selectively absorb circularly polarized light propagating inside the PCCs. Through simulations with various designs, we analyzed the transmittance spectra, mode and ellipticity profiles of the chiral PCCs. In an optimized structure, we achieved a THz chiral PCC with a chiral mode at approximately 0.42 THz in a low magnetic field of around 0.2 T. The Q factor of the cavity remains high (>400), with a uniformly circularly polarized cavity electric field in the lateral plane of the central defect layer surfaces, which is ideal for integrating two-dimensional materials and thin film samples. Furthermore, we demonstrated the feasibility of our THz chiral PCC for investigating cavity-dressed materials by estimating the Dirac gap size induced in graphene due to its coupling with the chiral cavity, based on a microscopic model. Our calculations indicate that the estimated gap reaches approximately 1 meV, with the potential for enhancement through further reduction of the cavity mode volume.

Results

Chiral 1D-PCC: Design Principle and Optimum Structure

Let us first consider a conventional 1D-PCC composed of five silicon layers (i)–(v) separated by air, as depicted in Fig. 2a. The refractive indices of the layers at THz frequencies are $n_{\text{Si}} = 3.42$ and $n_{\text{air}} = 1$. The layer thicknesses are $d_{\text{Si}} = 50\,\mu\text{m}$ and $d_{\text{air}} = 198\,\mu\text{m}$. Layer (iii) is twice as thick as the other layers, acting as a defect layer in the 1D-PCC. We used COMSOL Multiphysics 6.2 to calculate the normalized power, P, of transmitted THz radiation for different polarizations ($+$ for LCP and $-$ for RCP), as shown in Fig. 2b. The incident THz beam is linearly polarized in the x direction. Figure 2b reveals a high-Q defect mode ($Q = 493$) at $\omega_{\text{cav}}/2\pi = 0.423\,\text{THz}$ within the photonic band gap between around 0.25 and 0.55 THz.

As the conventional 1D-PCC is not chiral, the transmitted light remains linearly polarized in the x direction ($P_x \approx 1$, $P_y = 0$, and $P_+ = P_- \approx 0.5$). Figure 2c displays the spatial profiles of the cavity electric field in the $-$ polarization, $|E_-(z)| = |(E_x(z) - iE_y(z))/\sqrt{2}|$, and ellipticity, $\eta(z) = \frac{|E_-(z)|-|E_+(z)|}{|E_-(z)|+|E_+(z)|}$, at the peak frequency of the 1D-PCC. The electric field is linearly (circularly) polarized if $\eta(z) = 0$ ($\eta(z) = \pm 1$). At the mode frequency, the electric field is highly localized near the surfaces of the defect layer, z_{max}, with $\eta = 0$ across the cavity. This conventional 1D-PCC design has been utilized to achieve ultrastrong coupling by placing an ultrahigh-mobility two-dimensional electron gas at z_{max} [26, 27].

Next, we consider replacing specific silicon layers in the 1D-PCC with lightly-doped n-InSb layers. Lightly-doped n-InSb contains a low-density plasma with plasma frequency in the THz frequency range, and a magnetoplasma with nonreciprocity properties is formed

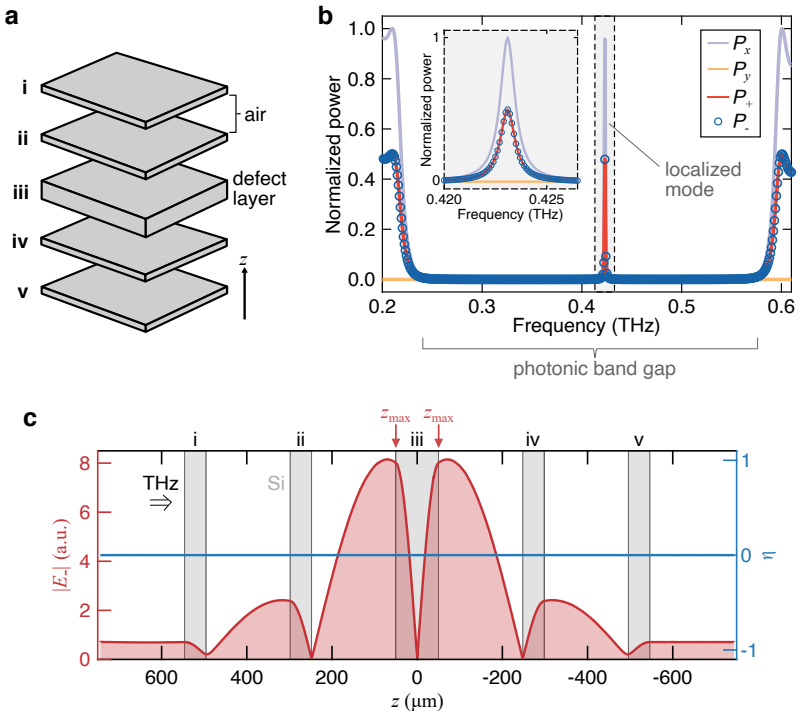

Fig. 2 A conventional 1D-PCC. a, Schematic diagram of the 1D-PCC. It consists of five layers, labeled layers (i)–(v), separated by a 198-μm-thick air gap. Layer (iii) is the defect layer with a thickness of 100 μm, which is thicker than the other layers (50 μm). **b**, Normalized power (P) spectra of transmitted light for different polarizations. The incident light is linearly polarized along the x axis. The inset is a magnified view of the spectrum. **c**, The spatial profiles of the circularly polarized electric field ($|E_-|$) and ellipticity (η) at the cavity mode frequency. The grey rectangles represent the positions of the silicon layers. Light is incident from the left side. $z_{\max}$ denotes the surfaces of the defect layer where the electric field reaches its maximum.

when an external magnetic field, B, is applied. The complex permittivity of the magneto-plasma at B is given by a gyrotropic permittivity tensor [28, 29]

$$\tilde{\varepsilon} = \begin{pmatrix} \varepsilon_{xx}(\omega) & \varepsilon_{xy}(\omega) & 0 \\ -\varepsilon_{xy}(\omega) & \varepsilon_{xx}(\omega) & 0 \\ 0 & 0 & \varepsilon_{zz} \end{pmatrix}, \tag{1}$$

with

$$\varepsilon_{xx}(\omega) = \varepsilon_{\mathrm{bg}} - \frac{\omega_{\mathrm{p}}^2(\omega - i\gamma)}{\omega[(\omega - i\gamma)^2 - \omega_{\mathrm{c}}^2]}, \tag{2}$$

$$\varepsilon_{xy}(\omega) = \frac{-i\omega_{\mathrm{p}}^2\omega_{\mathrm{c}}}{\omega[(\omega - i\gamma)^2 - \omega_{\mathrm{c}}^2]}, \tag{3}$$

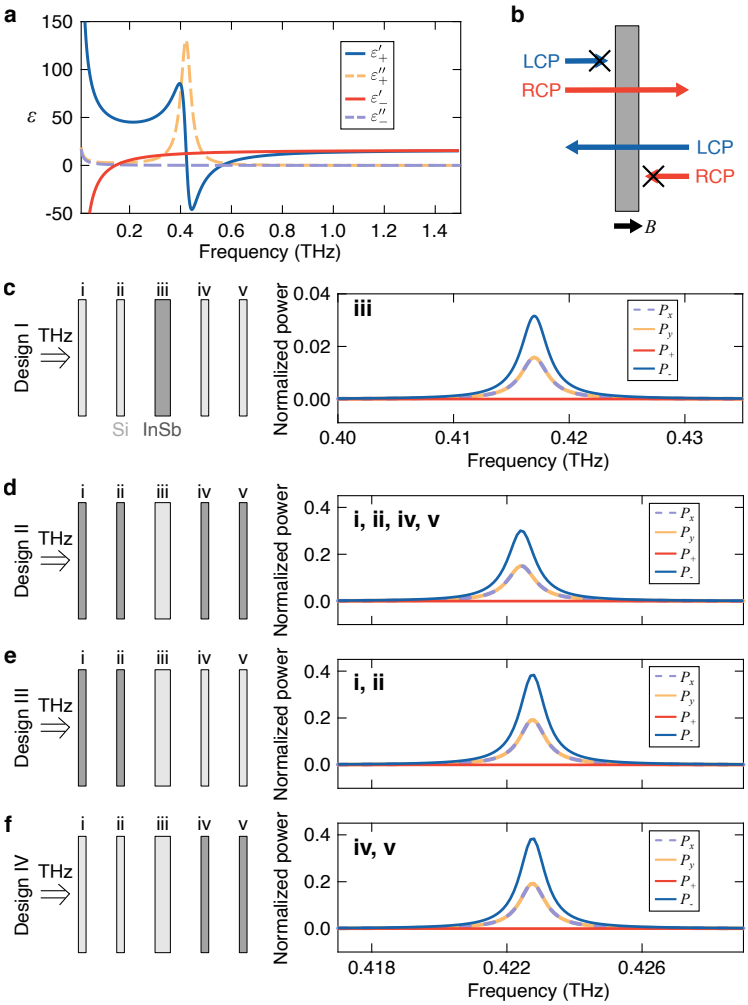

Fig. 3 Nonreciprocal THz magnetoplasma in lightly doped InSb and its incorporation into a 1D-PCC. a, Complex permittivity, $\tilde{\varepsilon}_{\pm} = \varepsilon'_{\pm} - i\varepsilon''_{\pm}$, of the magnetoplasma in the circular basis at a magnetic field of $B = 0.212\,\mathrm{T}$, where light propagates in the same direction as B (Faraday geometry). **b**, Schematic diagram illustrating nonreciprocal transmission of circularly polarized light through the magnetoplasma. Blue and red arrows indicate the propagation direction of LCP and RCP light, respectively. When the propagation direction aligns with (opposes) the B direction, denoted by the black arrow, only RCP (LCP) light can transmit through the InSb layer. **c–f**, Normalized power (P) spectra for transmitted light for different polarizations. The incident THz beam is linearly polarized in the x direction. The left panels illustrate the configuration of four different designs (I–IV), with light and dark rectangles representing Si and InSb layers, respectively. Labels (i)–(v) in the right panels denote the layers that are InSb.

$$\varepsilon_{zz} = \varepsilon_{\mathrm{bg}} - \frac{\omega_{\mathrm{p}}^2}{\omega(\omega - i\gamma)}, \tag{4}$$

where ε_{bg} represents the background permittivity, $\omega_{\text{p}} = \sqrt{n_{\text{e}}e^2/(\varepsilon_0 m_{\text{eff}})}$ is the plasma frequency, n_{e} denotes the electron density, e is the electronic charge, ε_0 is the permittivity of free space, m_{eff} is the effective mass of the electrons, γ is the scattering rate, and $\omega_{\text{c}} = eB/m_{\text{eff}}$ is the cyclotron frequency. The magnetoplasma parameters we used in this study are similar to those reported in previous experimental studies [30, 31]: $n_{\text{e}} = 2.3 \times 10^{14}\,\text{cm}^{-3}$, $m_{\text{eff}} = 0.014m$ (where $m = 9.11 \times 10^{-31}\,\text{kg}$ is the free electron mass in vacuum), and $\gamma = 1.5 \times 10^{11}\,\text{rad/s}$.

Figure 3a displays the complex permittivity of the magnetoplasma in the circular basis, $\tilde{\varepsilon}_{\pm} = \varepsilon'_{\pm} - i\varepsilon''_{\pm}$, at $B = 0.212\,\text{T}$, where $\omega_{\text{cav}} = \omega_{\text{c}}$. $\tilde{\varepsilon}_{+}$ shows a Lorentzian peak at ω_{c}, indicating absorption of LCP radiation. By contrast, the magnetoplasma transmits RCP light at ω_{c} because $\varepsilon'_{-} > 0$ and $\varepsilon''_{-} \approx 0$. Due to the breaking of TRS by the external B, the roles of LCP and RCP light interchange when the propagation direction is reversed [Fig. 3b]. Specifically, RCP light is absorbed, while LCP light can pass through the InSb layer in this case.

The nonreciprocal nature of transmission through the magnetoplasma allows an InSb layer in B to selectively absorb specific circular polarized light depending on the propagation direction. This property of InSb can be utilized in a 1D-PCC design, because it can maintain counterpropagating waves with opposite handedness inside PCCs. Therefore, the defect mode of the PCC becomes chiral when $\omega_{\text{cav}} = \omega_{\text{c}}$. The low m_{eff} in InSb is advantageous for creating THz chiral PCCs because it requires only a small B to shift ω_{c} into the THz range. Furthermore, from Fig. 3a, we can see that $\varepsilon'_{-} \simeq 12.3$ at ω_{cav}, which is comparable to the permittivity of silicon. Therefore, replacing silicon layers with InSb layers does not significantly alter the photonic band gap and the frequency of the defect mode of the PCCs. Note that $\varepsilon'_{-} < 0$ when n_{e} is higher, imposing a limit on the maximum n_{e} feasible for achieving a chiral 1D-PCC.

In this study, we consider four different configurations of chiral 1D-PCCs, as shown in Fig. 3c–f.

- Design I: only layer (iii) (the defect layer) is InSb;
- Design II: all layers, except layer (iii), are InSb;
- Design III: only layers (i) and (ii) are InSb;
- Design IV: only layers (iv) and (v) are InSb.

First, we investigate the structure in Design I [Fig. 3c]. The transmittance spectrum of this structure has been previously studied [32–34]. Although the incident light is linearly polarized in the x direction, the transmitted light becomes fully circularly polarized as $P_+ \approx 0, P_- \approx 2P_x = 2P_y$. However, the amplitude of the defect mode in the transmittance spectrum significantly decreases (< 0.04), and the peak broadens ($Q = 146$). The peak frequency slightly decreases as well. Next, for the structure in Design II, the transmitted light remains circularly polarized as $P_+ \approx 0$ and $P_- \approx 2P_x = 2P_y$, as shown in Fig. 3d. However, the amplitude of the peak for P_- is much higher ($\simeq 0.3$). The Q factor of the cavity is approximately 427, which is comparable to that of a conventional 1D-PCC. Finally, we considered structures where only the first two layers [Design III] or the last two layers [Design IV] are replaced by InSb. The transmittance spectra are identical for both cases, as shown in Fig. 3e,f. The amplitude of the peaks increases further, and the Q factor reaches 458, while the transmitted light remains circularly polarized.

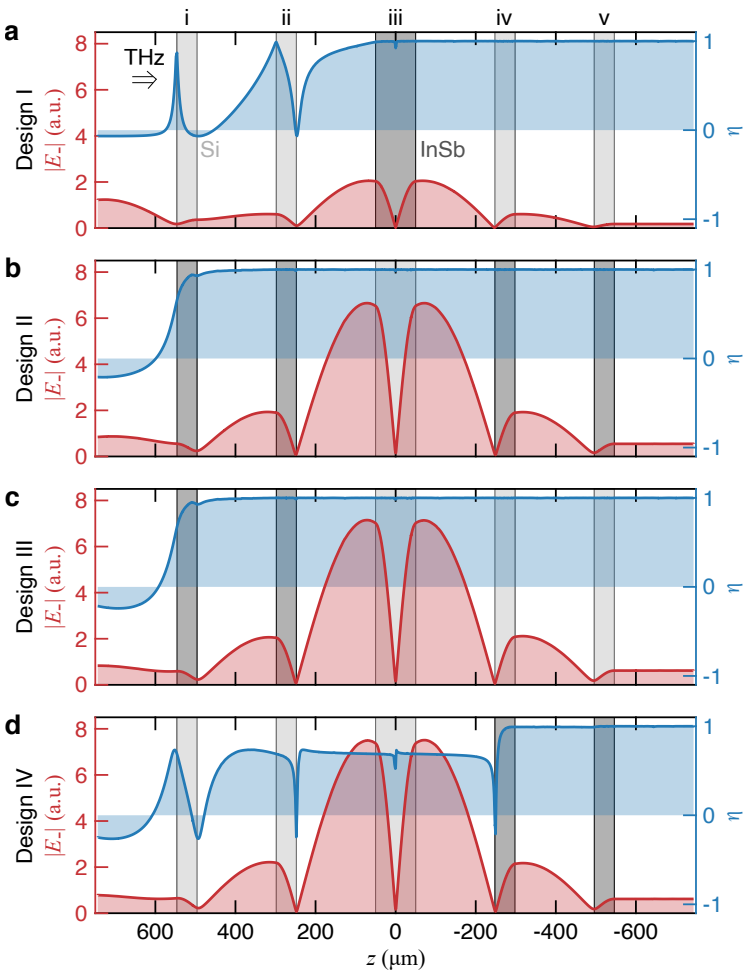

Fig. 4 Cavity electric field profiles of THz chiral 1D-PCCs. a–d, Mode and ellipticity profiles of chiral cavities in four different designs (I-IV). The red and blue traces represent the cavity electric field $|E_-|$ and ellipticity, η, respectively. The light and dark rectangles represent Si and InSb layers, respectively, that compose the 1D-PCCs. The following layers are InSb in the different designs: (**a**) iii; (**b**) i, ii, iv, v; (**c**) i, ii; (**d**) iv, v. The THz beam is incident from the left side and linearly polarized in the x direction.

In addition to achieving circular dichroism, our primary goal is to enhance circularly polarized vacuum electric fields. To examine this, we investigate the spatial profiles of $|E_-(z)|$ and $\eta(z)$ in four different designs, as shown in Fig. 4; the incident light is linearly polarized in the x direction. Note that all four designs exhibit $|E_-(z)|$ profiles similar to those of conventional 1D-PCCs, with maximum E_- occurring at the surfaces of the defect

layer. However, the transmitted power and the cavity electric field of the PCCs are particularly sensitive to losses in the defect layer compared to losses in other layers; see Supplement 1 for supporting content. Thus, the amplitude of $|E_{-}(z)|$ in Design I significantly decreases [Fig. 4a]. By contrast, the peak amplitude of $|E_{-}(z)|$ in Design II remains high [Fig. 4b]. Furthermore, the $\eta(z)$ profile suggests that the electric field becomes circularly polarized behind layer (ii) ($\eta(z) \simeq 1$), indicating an enhanced circularly polarized electric field at z_{max} in our chiral PCCs.

The transmittance spectra suggest that the Q factor of the chiral mode in Designs III and IV is higher. However, $\eta(z) < 1$ at z_{max} if light passes through the defect layer prior to the InSb layers [Fig. 4d]. Given that vacuum fields can approach from either side of the cavity, we conclude that the optimized chiral 1D-PCC design, which has broken TRS and features enhanced chiral vacuum fields, is Design II, which is depicted in Fig. 4b: a five-layer PCC composed of air and InSb layers with a silicon defect layer in the middle.

The presence of a magnetoplasma in InSb causes significant changes in both the transmittance spectra and mode profiles of our chiral PCCs as B is varied, see Supplement 1 for supporting content. At $B \neq 0.212\,\text{T}$, $\eta(z) < 1$ at z_{max} as ω_{c} is detuned from ω_{cav}. Furthermore, the handedness of the chiral resonance reverses when the sign of B is inverted.

Finally, we calculated the spatial profile of vacuum fluctuations of the chiral mode in the chiral PCCs by normalizing the mode profiles obtained from numerical simulations with circularly polarized incident THz beams; see Supplement 1 for supporting content. The circularly polarized vacuum field strength, $|E_{\text{vac,-}}|$ at z_{max} is approximately $1.35 \times 10^{-4}/\sqrt{S}$ V/m [Fig. 5a], where S denotes the surface area of the cavity. In addition, our approach can be utilized to realize chiral Tamm cavities for reflection measurements. A Tamm cavity is a combination of a photonic crystal and a metallic mirror [35]. We considered the chiral Tamm cavity structure with two InSb layers and a silicon layer coated with gold. The transmittance spectra and mode profiles of linear and chiral Tamm cavities are discussed in Supplement 1. Figure 5b displays the vacuum field profile of the chiral Tamm cavity. The amplitude of $|E_{\text{vac,-}}|$ increases to $1.92 \times 10^{-4}/\sqrt{S}$ V/m at z_{max}, while $\eta(z_{\text{max}}) \simeq 1$.

Advantages of Our Chiral PCCs

Our chiral PCC designs offer several advantages compared to previously reported chiral cavities with broken TRS [23–25]. First, the required B for our chiral PCCs is relatively low ($\sim 0.2\,\text{T}$) due to the low m_{eff} of electrons in InSb. This minimizes changes in the material properties induced solely by the external B. Second, the cavity electric field is uniformly circularly polarized in the xy plane. Third, the Q factors of the chiral PCCs remain high ($Q > 400$). Fourth, the defect layer in the optimum design (Design II), which serves as the substrate for materials embedded within the cavity, is made of silicon. This choice helps eliminate potential parasitic effects that could arise if the material were placed on a metallic substrate. Moreover, the mode volumes of the chiral PCCs can potentially be reduced by integrating air slots or bowtie structures into the multilayer design [36] or by coupling metasurface resonators with the chiral PCC [37, 38]. Two-dimensional materials and thin film samples can be conveniently embedded in the chiral PCCs to examine the effects of chiral vacuum fields on material properties in the vacuum state. Below we estimate the gap at the Dirac nodes of monolayer graphene placed inside our chiral PCC.

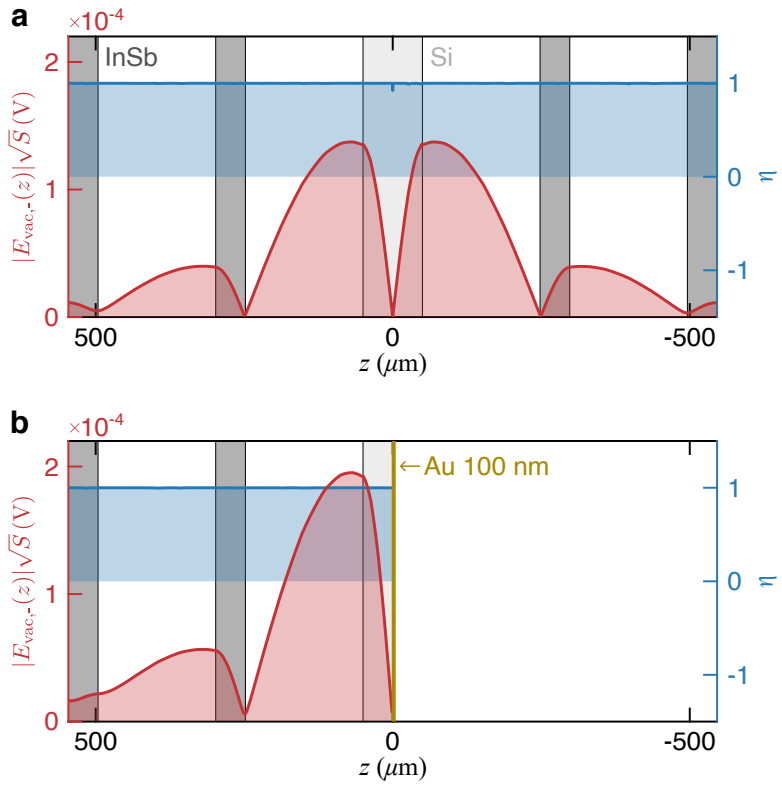

Fig. 5 Spatial profiles of the circular component of cavity electric fields in the vacuum state. a–b, The vacuum electric field profile, $|E_{\text{vac,-}}(z)|\sqrt{S}$, for (**a**) the chiral 1D-PCC and (**b**) the chiral Tamm cavity, where S represents the surface area of the cavity. The light and dark rectangles denote Si and InSb layers, respectively. The yellow line in (**b**) represents the gold layer. The definition of $|E_{\text{vac,-}}(z)|$ is discussed in Supplement 1.

Time-Reversal Symmetry in Hybrid Photo-Electronic Systems

Here, we briefly review how TRS is manifested in systems where charged particles are coupled to the quantized cavity fields. For a single electron in a periodic crystal potential coupled to light, the minimal coupling Hamiltonian [39, 40] follows as,

$$\mathcal{H} = \frac{1}{2m}\left(\mathrm{i}\hbar\nabla + e\mathbf{A}\right)^2 + V_{\text{crys}}(\mathbf{r}) + \sum_{\lambda=x,y} \hbar\omega_{\text{cav}}\left(b_\lambda^\dagger b_\lambda + \frac{1}{2}\right), \tag{5}$$

with a single cavity mode $\omega_{\text{cav}} = c|\kappa_z|$ where κ_z is photon wave number along the z direction, and m is the bare electron mass. Under this choice the polarizations of the cavity field are in the (x, y) plane. The operators $b_\lambda^\dagger, b_\lambda$ are the creation and annihilation operators of the photon field satisfying bosonic commutation relations $[b_\lambda, b_{\lambda'}^\dagger] = \delta_{\lambda\lambda'}$, and $V_{\text{crys}}(\mathbf{r})$ is the crystal

potential of graphene. For two-dimensional materials whose thickness is at the order of a single or a few atoms [41, 42], the cavity field in the z direction of our chiral PCC is taken to be uniform, see Fig. 4 where the 2D material will be placed on either side of the defect layer. Hence the vector potential reads,

$$\mathbf{A} = \sqrt{\frac{\hbar}{\varepsilon_0 \mathcal{V} 2\omega_{\text{cav}}}} \sum_{\lambda=x,y} \mathbf{e}_\lambda \left(b_\lambda^\dagger + b_\lambda \right), \tag{6}$$

where $\mathcal{V}$ is the effective mode volume, $\mathbf{e}_x$ and $\mathbf{e}_y$ are the linear polarization vectors of light.

In classical physics, the momentum $\mathbf{p}$ of a particle and the classical vector potential $\mathbf{A}_{\text{cl}}(t)$ transform under time-reversal $\mathcal{T}$ as $\mathcal{T}(\mathbf{p}) = -\mathbf{p}$ and $\mathcal{T}(\mathbf{A}_{\text{cl}}) = -\mathbf{A}_{\text{cl}}$ [43], such that a linearly polarized electric field $\mathbf{E}_{\text{cl}}(t)$ is invariant under TRS. These transformation rules must be preserved under quantization leading to $\mathcal{T}(-\mathrm{i}\hbar\nabla) = \mathrm{i}\hbar\nabla$ and $\mathcal{T}(\mathbf{A}) = -\mathbf{A}$. Under this transformation $\{b_{x,y}, b_{x,y}^\dagger\}$ have to satisfy $\mathcal{T}(b_{x,y}) = -b_{x,y}$ and $\mathcal{T}(b_{x,y}^\dagger) = -b_{x,y}^\dagger$. With the use of these relations we can find that the photon number operator $b_\lambda^\dagger b_\lambda$ is invariant under TRS $\mathcal{T}(b_\lambda^\dagger b_\lambda) = b_\lambda^\dagger b_\lambda$ for linearly polarized light. By combining all transformation rules, we find that the minimal coupling Hamiltonian for linearly polarized light is invariant under TRS $\mathcal{T}(\mathcal{H}) = \mathcal{H}$.

To discuss TRS under circular polarization, we make a basis change in the polarization vectors from $\mathbf{e}_x$ and $\mathbf{e}_y$ to left $\mathbf{e}_L = (1, -\mathrm{i})/\sqrt{2}$ and right $\mathbf{e}_R = (1, \mathrm{i})/\sqrt{2}$ circular polarizations through the expressions $\mathbf{e}_x = (\mathbf{e}_R + \mathbf{e}_L)/\sqrt{2}$ and $\mathbf{e}_y = -\mathrm{i}(\mathbf{e}_R - \mathbf{e}_L)/\sqrt{2}$ [44]. Then the photon field takes the form

$$\mathbf{A} = \sqrt{\frac{\hbar}{\varepsilon_0 \mathcal{V} 2\omega_{\text{cav}}}} \left[\mathbf{e}_R b_L + \mathbf{e}_R b_R^\dagger + \mathbf{e}_L b_R + \mathbf{e}_L b_L^\dagger \right], \tag{7}$$

where we defined the photon operators for left and right circularly polarized photons as linear combinations of the linearly polarized ones, $b_L = \frac{1}{\sqrt{2}} (b_x - \mathrm{i} b_y)$ and $b_R = \frac{1}{\sqrt{2}} (b_x + \mathrm{i} b_y)$. It can be checked that the left and right-handed photon operators satisfy standard bosonic commutation relations $[b_L, b_L^\dagger] = [b_R, b_R^\dagger] = 1$, and are independent $[b_L, b_R^\dagger] = 0$. Using the definition of the left and right polarized photon operators, we find their transformation under TRS to be

$$\mathcal{T}(b_{L,R}) = -b_{R,L} \text{ and } \mathcal{T}(b_{L,R}^\dagger) = -b_{R,L}^\dagger. \tag{8}$$

Thus, we see that TRS exchanges left and right photon operators (up to a minus). The same also holds for left and right polarization vectors $\mathcal{T}(\mathbf{e}_R) = \mathbf{e}_L$ and $\mathcal{T}(\mathbf{e}_L) = \mathbf{e}_R$. Hence, expectantly $\mathcal{T}(\mathbf{A}) = -\mathbf{A}$ still holds, while the energy of the photon field in terms of left and right circularly polarized operators takes the standard form $\sum_{\lambda=x,y} \hbar\omega_{\text{cav}} \left(b_\lambda^\dagger b_\lambda + \frac{1}{2} \right) = \sum_{\lambda=L,R} \hbar\omega_{\text{cav}} \left(b_\lambda^\dagger b_\lambda + \frac{1}{2} \right)$, being invariant under TRS, too. If the right circularly polarized photons are completely absorbed by the magnetoplasma in InSb, the cavity field would read

$$\mathbf{A}_L = \sqrt{\frac{\hbar}{\varepsilon_0 \mathcal{V} 2\omega_{\text{cav}}}} \left[\mathbf{e}_R b_L + \mathbf{e}_L b_L^\dagger \right]. \tag{9}$$

It is straightforward to see $\mathcal{T}(\mathbf{A}_L) = -\mathbf{A}_R$ breaking TRS. Let us note that even when the absorption of one polarization by InSb is imperfect, we would still have a field of the form $\mathbf{A}' = \alpha_L \mathbf{A}_L + \alpha_R \mathbf{A}_R$ where $\alpha_R \neq \alpha_L$, and hence the TRS is still broken, $\mathcal{T}(\mathbf{A}') \neq -\mathbf{A}'$ [10].

Tight-binding Model with Density Functional Theory and Dirac Gap Estimation

Next, we derive the tight-binding Hamiltonian for graphene coupled to our single polarization chiral PCC. The study of monolayer graphene strongly coupled to chiral cavity modes has attracted considerable interest in recent years [10, 45–48]. Here, we will follow the approach developed in Ref. [10] and extend it further by including ab-initio calculations for the graphene monolayer. Expanding the covariant kinetic energy in the minimal-coupling Hamiltonian in Eq. (5), we have

$$\mathcal{H} = \underbrace{-\frac{\hbar^2}{2m}\nabla^2 + V_{\text{crys}}(\mathbf{r})}_{\text{Matter: } \mathcal{H}_{\text{m}}} + \underbrace{\frac{ie\hbar}{m}\mathbf{A}\cdot\nabla}_{\text{Photon-Matter: } \mathcal{H}_{\text{pm}}} + \underbrace{\frac{e^2}{2m}\hat{\mathbf{A}}^2 + \hbar\omega_{\text{cav}}\left(b_L^\dagger b_L + \frac{1}{2}\right)}_{\text{Photonic: } \mathcal{H}_p}. \tag{10}$$

where the external potential is periodic under Bravais lattice translations $V_{\text{crys}}(\mathbf{r} + \mathbf{R_j}) = V_{\text{crys}}(\mathbf{r})$ with $\mathbf{R_j}$ being the Bravais lattice vectors [49]. Substituting the expression for the vector potential $\mathbf{A}_L$ and introducing the diamagnetic frequency $\omega_{\text{D}} = \sqrt{\frac{e^2}{m\varepsilon_0\mathcal{V}}}$ the photonic Hamiltonian $\mathcal{H}_p$ takes the form

$$\mathcal{H}_p = \hbar\omega_{\text{cav}}\left(b_L^\dagger b_L + \frac{1}{2}\right) + \frac{\hbar\omega_{\text{D}}^2}{4\omega_{\text{cav}}}\left(b_L + b_L^\dagger\right)^2. \tag{11}$$

Now $\mathcal{H}_p$ can be brought into diagonal form by introducing a new set of bosonic operators: $a_L^\dagger$ and a_L

$$a_L = \frac{1}{2\sqrt{\omega_{\text{cav}}\omega}}\left[b_L\left(\omega + \omega_{\text{cav}}\right) + b_L^\dagger\left(\omega - \omega_{\text{cav}}\right)\right] \quad \text{with} \quad \omega = \sqrt{\omega_{\text{cav}}^2 + \omega_{\text{D}}^2}. \tag{12}$$

The frequency ω is the dressed cavity frequency which depends on the bare cavity frequency ω_{cav} and the diamagnetic shift ω_{D} [50], and the operators $a_L, a_L^\dagger$ satisfy bosonic commutation relations $[a_L, a_L^\dagger] = 1$. Then $\mathcal{H}_p$ and $\mathbf{A}_L$ can be simply written as

$$\mathcal{H}_p = \hbar\omega\left(a_L^\dagger a_L + \frac{1}{2}\right), \qquad \mathbf{A}_L = \left(\frac{\hbar}{\varepsilon_0\mathcal{V}}\right)^{\frac{1}{2}}\frac{1}{\sqrt{2\omega}}\left(\mathbf{e}_R a_L + \mathbf{e}_L a_L^\dagger\right). \tag{13}$$

Graphene has two sublattices, A and B, and as a consequence, the tight-binding ansatz wavefunction consists of two components, one for each sublattice [51],

$$\Psi_{\mathbf{k}}(\mathbf{r}) = a_{\mathbf{k}}\Psi_{\mathbf{k}}^A(\mathbf{r}) + b_{\mathbf{k}}\Psi_{\mathbf{k}}^B(\mathbf{r}) = \sum_{\mathbf{j}} e^{i\mathbf{k}\cdot\mathbf{R_j}}\left[a_{\mathbf{k}}\phi_A(\mathbf{r} - \mathbf{R_j}) + b_{\mathbf{k}}\phi_B(\mathbf{r} - \mathbf{R_j^B})\right], \tag{14}$$

where $\mathbf{R_j} = j_1\mathbf{a}_1 + j_2\mathbf{a}_2$ are the Bravais vectors of sublattice A with $\mathbf{a}_1 = \mathbf{e}_x\alpha\sqrt{3}/2 + \mathbf{e}_y 3\alpha/2$ and $\mathbf{a}_2 = -\mathbf{e}_x\alpha\sqrt{3}/2 + \mathbf{e}_y 3\alpha/2$, where α is the graphene lattice constant. The Bravais vectors for the sublattice B are $\mathbf{R}_\mathbf{j}^B = \mathbf{R_j} + \boldsymbol{\delta}_3$ with $\boldsymbol{\delta}_3 = -\alpha\mathbf{e}_y$. To derive the tight-binding Hamiltonian we apply $\mathcal{H}$ to Eq. (14)

$$\mathcal{H}_\mathbf{k} = \begin{pmatrix} \langle\Psi_\mathbf{k}^A|\mathcal{H}|\Psi_\mathbf{k}^A\rangle & \langle\Psi_\mathbf{k}^A|\mathcal{H}|\Psi_\mathbf{k}^B\rangle \\ \langle\Psi_\mathbf{k}^A|\mathcal{H}|\Psi_\mathbf{k}^B\rangle^* & \langle\Psi_\mathbf{k}^B|\mathcal{H}|\Psi_\mathbf{k}^B\rangle \end{pmatrix}. \tag{15}$$

The tight-binding Hamiltonian of graphene, $\langle\Psi_\mathbf{k}^A|\mathcal{H}_m|\Psi_\mathbf{k}^B\rangle = t\left[1 + e^{\mathrm{i}\mathbf{k}\cdot\mathbf{a}_1} + e^{\mathrm{i}\mathbf{k}\cdot\mathbf{a}_2}\right]$, can be derived from the ansatz Eq. (14) [49, 51] (also see the review of this in SI Sec. 6.). Here t can be found by density functional theory (DFT) as $t = 2.8$eV [52]. Now we apply $\mathcal{H}_\mathrm{pm}$ to Eq. (14)

$$\mathcal{H}_\mathbf{k}^\mathrm{pm} = \begin{pmatrix} \langle\Psi_\mathbf{k}^A|\mathcal{H}_\mathrm{pm}|\Psi_\mathbf{k}^A\rangle & \langle\Psi_\mathbf{k}^A|\mathcal{H}_\mathrm{pm}|\Psi_\mathbf{k}^B\rangle \\ \langle\Psi_\mathbf{k}^A|\mathcal{H}_\mathrm{pm}|\Psi_\mathbf{k}^B\rangle^* & \langle\Psi_\mathbf{k}^B|\mathcal{H}_\mathrm{pm}|\Psi_\mathbf{k}^B\rangle \end{pmatrix}. \tag{16}$$

We neglect the diagonal terms which results in tunneling between sites beyond nearest neighbors. Thus, we only need to compute $\mathrm{i}\hbar\langle\Psi_\mathbf{k}^A|\nabla|\Psi_\mathbf{k}^B\rangle$. In Ref. [10], an analytic perturbative approach with respect to the graphene lattice constant was followed for the derivation of the light-matter interaction term and its strength. Here, in order to make a more realistic prediction for cavity-induced Dirac gap, we incorporate ab-initio DFT simulations, which can provide the transition matrix elements between valence and conductions bands $-\mathrm{i}\hbar\langle\Psi_\mathbf{k}^v|\nabla|\Psi_\mathbf{k}^c\rangle$ for graphene monolayer (see SI Sec. 7 for details), where v and c stand for valence and conduction bands, respectively. With a basis change from valence and conduction bands to A and B sublattices for the bare graphene, we find the relation

$$\mathrm{i}\hbar\langle\Psi_\mathbf{k}^A|\nabla|\Psi_\mathbf{k}^B\rangle = -\sqrt{2}\frac{\left[1 + e^{\mathrm{i}\mathbf{k}\cdot\mathbf{a}_1} + e^{\mathrm{i}\mathbf{k}\cdot\mathbf{a}_2}\right]}{\left|1 + e^{\mathrm{i}\mathbf{k}\cdot\mathbf{a}_1} + e^{\mathrm{i}\mathbf{k}\cdot\mathbf{a}_2}\right|}\mathrm{Re}\left[\mathrm{i}\hbar\langle\Psi_\mathbf{k}^v|\nabla|\Psi_\mathbf{k}^c\rangle\right]. \tag{17}$$

We focus only on the Dirac nodes, $\mathbf{K}$ and $\mathbf{K}'$, from now on to estimate the gap. The relation above simplifies to $\mathrm{i}\hbar\langle\Psi_\mathbf{K}^A|\nabla|\Psi_\mathbf{K}^B\rangle = -\sqrt{2}\mathrm{Re}\left[\mathrm{i}\hbar\langle\Psi_\mathbf{k}^v|\nabla|\Psi_\mathbf{k}^c\rangle\right]$ at the Dirac nodes. Hence, the light–matter interaction Hamiltonian at the Dirac node reads,

$$\mathcal{H}_\mathbf{K}^\mathrm{pm} = \frac{e}{m}\begin{pmatrix} 0 & \mathbf{A}_L\cdot\mathrm{i}\hbar\langle\Psi_\mathbf{K}^A|\nabla|\Psi_\mathbf{K}^B\rangle \\ -\mathbf{A}_L\cdot\mathrm{i}\hbar\langle\Psi_\mathbf{K}^A|\nabla|\Psi_\mathbf{K}^B\rangle^* & 0 \end{pmatrix}. \tag{18}$$

Remembering $\mathbf{A}_L$ in Eq. (13), we can define a light–matter coupling constant as

$$g = \frac{e}{m}\sqrt{\frac{2\pi}{\mathcal{V}\omega}}. \tag{19}$$

Effective cavity volume visible to graphene will be affected by the refractive index of the defect layer $\mathcal{V} = \chi\left(\frac{2\pi c}{\omega_\mathrm{cav} n_\mathrm{Si}}\right)^3$ where c is the speed of light, and χ is the light confinement parameter [5], and since there is confinement in only one direction in our PCC, $\chi = 0.1034$. Although this leads to a relatively small $g \sim 8\times10^{-8}$a.u., the matrix element $\langle\Psi_\mathbf{K}^A|\nabla|\Psi_\mathbf{K}^B\rangle$ at

the Dirac nodes enhances the light–matter interaction due to linear dispersion leading to a gap of 0.88 meV. This gap strength can be further enhanced by engineering the light confinement within the chiral PCCs. One promising approach is to couple metasurface resonators with the chiral PCCs [37, 38]. For example, one can achieve $\chi \sim 3.2 \times 10^{-4}$ with this approach leading to $g = 1.4 \times 10^{-6}$ and a gap of ~ 2 meV. By increasing the cavity frequency to $\omega_{\mathrm{cav}} = 2$ THz, one can obtain a gap on the order of 10 meV.

Discussion and Outlook

In this study, we proposed and analyzed chiral PCCs with broken TRS. Unlike conventional PCCs, one of the dielectric media in our chiral PCCs is replaced by a lightly doped semiconductor such as InSb. The cavity resonance becomes chiral when the PCC mode frequency ω_{cav} overlaps with the cyclotron frequency of the magnetoplasma in InSb, ω_{c}. Thus, the required B for the chiral PCCs depends on m_{eff} of the magnetoplasma. Our findings indicate that the Q factor and the confined electric field strength inside the cavity remain almost unchanged if the defect layer remains dielectric. The optimized design is photonic crystals formed by air and InSb with a silicon defect layer in the middle (Design II). The ellipticity of the cavity electric field at the surfaces of the defect layer is approximately 1 and spatially uniform in the lateral direction. We also discussed the estimated gap size in graphene, which arises from its coupling to the chiral PCCs, based on the microscopic model. It is important to highlight that gaps on the order of 1 to 10 meV, like the ones we predict, are within the experimental range of cryogenic transport measurements [53, 54]. Recent studies have successfully conducted transport measurements in THz cavities to explore the influence of vacuum fluctuations on the quantum Hall effect [6, 55]. Thus, our proposal for a chiral photonic-crystal cavity with broken time-reversal symmetry, accompanied by the theoretical prediction for the topological gap at the Dirac nodes, suggests that a vacuum-induced topological Chern insulator in graphene can be potentially observed with the current technology [1, 9, 10]. The low-loss chiral PCCs with broken TRS are important for exploring modifications in the physical properties of quantum materials induced by chiral vacuum fields. Future work should focus on reducing the mode volume further to enhance the light-matter interaction strength by engineering the lateral structure of the chiral PCCs.

Supplementary information. Supplementary information is available for this paper at here.

Acknowledgements. We thank David Hagenmüller and Xiangfeng Wang for useful discussions.

Declarations

- Funding

  J.K. acknowledges support from the U.S. Army Research Office (through Award No. W911NF2110157), the Gordon and Betty Moore Foundation (through Grant No. 11520), the W. M. Keck Foundation (through Award No. 995764), and the Robert A. Welch Foundation (through Grant No. C-1509). V.R. and C.B.D. acknowledge support from National Science Foundation grant for ITAMP at Harvard University [Award No: 2116679].

- Conflict of interest/Competing interests

  The authors declare no competing interests.

- Ethics approval

  Not applicable.

- Consent to participate

  Not applicable.

- Consent for publication

  Not applicable.

- Data availability

  The numerical simulations that support the plots in this paper are available from the corresponding author upon reasonable request.

- Code availability

  The codes used in this study are available from the corresponding author upon reasonable request.

- Authors' contributions

  F.T., V.R., C.B.D., and J.K. conceptualized the project. F.T. designed the cavity and performed numerical simulations with input from S.S., A.B., A.A. V.R. and C.B.D. developed the microscopic model and performed calculations. Z.S. and D.M.W. performed DFT calculations. V.R., C.B.D., and J.K. supervised the project. F.T., V.R., C.B.D., and J.K. prepared the manuscript with inputs from all authors.

References

[1] Hübener, H. *et al.* Engineering quantum materials with chiral optical cavities. *Nat. Mater.* **20**, 438–442 (2021).

[2] Garcia-Vidal, F. J., Ciuti, C. & Ebbesen, T. W. Manipulating matter by strong coupling to vacuum fields. *Science* **373**, eabd0336 (2021).

[3] Schlawin, F., Kennes, D. M. & Sentef, M. A. Cavity quantum materials. *Appl. Phys. Rev.* **9**, 011312 (2022).

[4] Bloch, J., Cavalleri, A., Galitski, V., Hafezi, M. & Rubio, A. Strongly correlated electron–photon systems. *Nature* **606**, 41–48 (2022).

[5] Paravicini-Bagliani, G. L. *et al.* Magneto-transport controlled by Landau polariton states. *Nat. Phys.* **15**, 186–190 (2019).

[6] Appugliese, F. *et al.* Breakdown of topological protection by cavity vacuum fields in the integer quantum Hall effect. *Science* **375**, 1030–1034 (2022).

[7] Jarc, G. *et al.* Cavity-mediated thermal control of metal-to-insulator transition in 1T-TaS2. *Nature* **622**, 487–492 (2023).

[8] McIver, J. W. *et al.* Light-induced anomalous Hall effect in graphene. *Nat. Phys.* **16**, 38–41 (2020).

[9] Wang, X., Ronca, E. & Sentef, M. A. Cavity quantum electrodynamical Chern insulator: Towards light-induced quantized anomalous Hall effect in graphene. *Phys. Rev. B* **99**, 235156 (2019).

[10] Dag, C. B. & Rokaj, V. Engineering topology in graphene with chiral cavities. *Phys. Rev. B* **110**, L121101 (2024).

[11] Caloz, C. *et al.* Electromagnetic Nonreciprocity. *Phys. Rev. Appl.* **10**, 047001 (2018).

[12] Plum, E. & Zheludev, N. I. Chiral mirrors. *Appl. Phys. Lett.* **106**, 221901 (2015).

[13] Sun, S., Gu, B. & Mukamel, S. Polariton ring currents and circular dichroism of Mg-porphyrin in a chiral cavity. *Chem. Sci.* **13**, 1037–1048 (2022).

[14] Thiel, M., Rill, M. S., von Freymann, G. & Wegener, M. Three-Dimensional Bi-Chiral Photonic Crystals. *Adv. Mater.* **21**, 4680–4682 (2009).

[15] Thiel, M., Fischer, H., von Freymann, G. & Wegener, M. Three-dimensional chiral photonic superlattices. *Opt. Lett.* **35**, 166–168 (2010).

[16] Takahashi, S. *et al.* Circular dichroism in a three-dimensional semiconductor chiral photonic crystal. *Appl. Phys. Lett.* **105**, 051107 (2014).

[17] Semnani, B., Flannery, J., Al Maruf, R. & Bajcsy, M. Spin-preserving chiral photonic crystal mirror. *Light Sci. Appl.* **9**, 23 (2020).

[18] Voronin, K., Taradin, A. S., Gorkunov, M. V. & Baranov, D. G. Single-Handedness Chiral Optical Cavities. *ACS Photonics* (2022).

[19] Schäferling, M., Dregely, D., Hentschel, M. & Giessen, H. Tailoring Enhanced Optical Chirality: Design Principles for Chiral Plasmonic Nanostructures. *Phys. Rev. X* **2**, 031010 (2012).

[20] Wang, Z., Cheng, F., Winsor, T. & Liu, Y. Optical chiral metamaterials: A review of the fundamentals, fabrication methods and applications. *Nanotechnology* **27**, 412001 (2016).

[21] Hentschel, M., Schäferling, M., Duan, X., Giessen, H. & Liu, N. Chiral plasmonics. *Sci. Adv.* **3**, e1602735 (2017).

[22] Ma, W., Cheng, F. & Liu, Y. Deep-Learning-Enabled On-Demand Design of Chiral Metamaterials. *ACS Nano* **12**, 6326–6334 (2018).

[23] Suárez-Forero, D. G. *et al.* Chiral Optical Nano-Cavity with Atomically Thin Mirrors (2023). Preprint at arXiv, 2308.04574.

[24] Andberger, J. *et al.* Terahertz chiral subwavelength cavities breaking time-reversal symmetry via ultrastrong light-matter interaction. *Phys. Rev. B* **109**, L161302 (2024).

[25] Aupiais, I. *et al.* Chiral TeraHertz Surface Plasmonics. *ACS Photonics* (2024).

[26] Zhang, Q. *et al.* Collective non-perturbative coupling of 2D electrons with high-quality-factor terahertz cavity photons. *Nat. Phys.* **12**, 1005–1011 (2016).

[27] Li, X. *et al.* Vacuum Bloch–Siegert shift in Landau polaritons with ultra-high cooperativity. *Nat. Photon.* **12**, 324–329 (2018).

[28] Rajabali, S. *et al.* Polaritonic nonlocality in light–matter interaction. *Nat. Photon.* **15**, 690–695 (2021).

[29] Tay, F. *et al.* Multimode ultrastrong coupling in three-dimensional photonic-crystal cavities (2023). Preprint at arXiv, 2308.12427.

[30] Arikawa, T., Wang, X., Belyanin, A. A. & Kono, J. Giant tunable Faraday effect in a semiconductor magneto-plasma for broadband terahertz polarization optics. *Opt. Express* **20**, 19484–19492 (2012).

[31] Ju, X. *et al.* Creating a near-perfect circularly polarized terahertz beam through the nonreciprocity of a magnetoplasma. *Opt. Express* **31**, 38540–38549 (2023).

[32] Lee, K. J., Wu, J. W. & Kim, K. Defect modes in a one-dimensional photonic crystal with a chiral defect layer. *Opt. Mater. Express* **4**, 2542–2550 (2014).

[33] Aly, A. H., Elsayed, H. A., Ameen, A. A. & Mohamed, S. H. Tunable properties of one-dimensional photonic crystals that incorporate a defect layer of a magnetized plasma. *Int. J. Mod. Phys. B* **31**, 1750239 (2017).

[34] Li, T., Yin, C. & Wu, F. Strong optical non-reciprocity in one-dimensional photonic crystal containing a Weyl semimetal-based defect. *Opt. Mater.* **121**, 111583 (2021).

[35] Messelot, S. *et al.* Tamm Cavity in the Terahertz Spectral Range. *ACS Photonics* **7**, 2906–2914 (2020).

[36] Hu, S. *et al.* Experimental realization of deep-subwavelength confinement in dielectric optical resonators. *Sci. Adv.* **4**, eaat2355 (2018).

[37] Meng, F. *et al.* Nonlocal collective ultrastrong interaction of plasmonic metamaterials and photons in a terahertz photonic crystal cavity. *Opt. Express* **27**, 24455–24468 (2019).

[38] Messelot, S., Coeymans, S., Tignon, J., Dhillon, S. & Mangeney, J. High Q and sub-wavelength THz electric field confinement in ultrastrongly coupled THz resonators. *Photon. Res.* **11**, 1203 (2023).

[39] Spohn, H. *Dynamics of charged particles and their radiation field* (Cambridge university press, 2004).

[40] Cohen-Tannoudji, C., Dupont-Roc, J. & Grynberg, G. *Photons and Atoms-Introduction to Quantum Electrodynamics* (Wiley-VCH, 1997).

[41] Mak, K. F. & Shan, J. Semiconductor moiré materials. *Nat. Nanotechnol.* **17**, 686–695 (2022).

[42] Andrei, E. Y. *et al.* The marvels of Moiré materials. *Nat. Rev. Mater.* **6**, 201–206 (2021).

[43] Luo, R., Benenti, G., Casati, G. & Wang, J. Onsager reciprocal relations with broken time-reversal symmetry. *Phys. Rev. Res.* **2**, 022009 (2020).

[44] Baym, G. *Lectures on Quantum Mechanics* (W. A. Benjamin Inc., 1973).

[45] Kibis, O. V. Metal-insulator transition in graphene induced by circularly polarized photons. *Phys. Rev. B* **81**, 165433 (2010).

[46] Wang, X., Ronca, E. & Sentef, M. A. Cavity quantum electrodynamical chern insulator: Towards light-induced quantized anomalous hall effect in graphene. *Phys. Rev. B* **99**, 235156 (2019).

[47] Masuki, K. & Ashida, Y. Berry phase and topology in ultrastrongly coupled quantum light-matter systems. *Phys. Rev. B* **107**, 195104 (2023).

[48] Kibis, O. V., Kyriienko, O. & Shelykh, I. A. Band gap in graphene induced by vacuum fluctuations. *Phys. Rev. B* **84**, 195413 (2011).

[49] Aschroft, N. W. & Mermin, N. *Solid State Physics* (Harcourt College Publishers, 1976).

[50] Rokaj, V., Ruggenthaler, M., Eich, F. G. & Rubio, A. Free electron gas in cavity quantum electrodynamics. *Phys. Rev. Res.* **4**, 013012 (2022).

[51] Bena, C. & Montambaux, G. Remarks on the tight-binding model of graphene. *New J. Phys.* **11**, 095003 (2009).

[52] Castro Neto, A. H., Guinea, F., Peres, N. M. R., Novoselov, K. S. & Geim, A. K. The electronic properties of graphene. *Rev. Mod. Phys.* **81**, 109–162 (2009).

[53] Zhang, Y., Tan, Y.-W., Stormer, H. L. & Kim, P. Experimental observation of the quantum hall effect and berry's phase in graphene. *Nature* **438**, 201–204 (2005).

[54] Klitzing, K. v., Dorda, G. & Pepper, M. New method for high-accuracy determination of the fine-structure constant based on quantized hall resistance. *Phys. Rev. Lett.* **45**, 494–497 (1980).

[55] Enkner, J. *et al.* Testing the renormalization of the von klitzing constant by cavity vacuum fields. *Phys. Rev. X* **14**, 021038 (2024).

Supplementary Information: Terahertz chiral photonic-crystal cavities with broken time-reversal symmetry

Fuyang Tay[1,2], Stephen Sanders[1], Andrey Baydin[1,3], Zhigang Song[4], Davis M. Welakuh[5], Alessandro Alabastri[1,3], Vasil Rokaj[6,7,8], Ceren B. Dag[6,7], Junichiro Kono[1,3,9,10*]

[1*]Department of Electrical and Computer Engineering, Rice University, Houston, 77005, Texas, USA.
[2]Applied Physics Graduate Program, Smalley–Curl Institute, Rice University, Houston, 77005, Texas, USA.
[3]Smalley–Curl Institute, Rice University, Houston, 77005, Texas, USA.
[4]John A. Paulson School of Engineering and Applied Sciences, Harvard University, Cambridge, 02139, Massachusetts, USA.
[5]Max Planck Institute for the Structure and Dynamics of Matter, Luruper Chaussee 149 Hamburg, 22761, Germany.
[6]ITAMP, Harvard-Smithsonian Center for Astrophysics, Cambridge, 02138, Massachusetts, USA.
[7]Department of Physics, Harvard University, Cambridge, 02138, Massachusetts, USA.
[8]Department of Physics, Villanova University, Villanova, 19085, Pennsylvania, USA.
[9]Department of Physics and Astronomy, Rice University, Houston, 77005, Texas, USA.
[10]Department of Materials Science and NanoEngineering, Rice University, Houston, 77005, Texas, USA.

*Corresponding author(s). E-mail(s): kono@rice.edu;

Contents

S1 Chiral 1D-PCCs with five magnetoplasma layers

Fig. S1(a) and (b) show that the transmitted power and electric field are greatly suppressed if the chiral 1D-PCC consists of five InSb layers. Even if we reduce the thickness of the defect layer slightly to shift the peak frequency to the bare cavity mode frequency, the transmitted power and the electric field remain weak.

S2 Effects of losses in PCCs

According to the figure in the main text, $\tilde{\varepsilon}_- \approx 12.298 - 0.104i$ at ω_{cav}, which corresponds to $\tilde{n} = 3.507 - 0.015i$.

To understand why the transmitted power and confined electric field decrease significantly when layer (iii) is InSb, we used a transfer matrix method (TMM) to investigate transmittance spectra of 1D-PCCs with different values of losses. Note that the TMM used the $\tilde{n} = n + i\kappa$ convention, which is opposite to the convention for the complex permittivity. In the calculations, $n = 3.42$ for all layers, but the value of κ increases for different layers. Both n and κ are constant as a function of frequency. Figure S2(a) shows the spectra when the κ of the defect layer (layer (iii)) increases, while Fig. S2(b) shows the spectra when the κ for all other layers (layer (i)–(ii) & (iv)–(v)) increases. The calculations show that the transmitted power is more sensitive to the losses in the defect layer than the losses in other layers. Thus, the transmitted power and the confined electric field are much lower when layer (iii) is replaced with InSb.

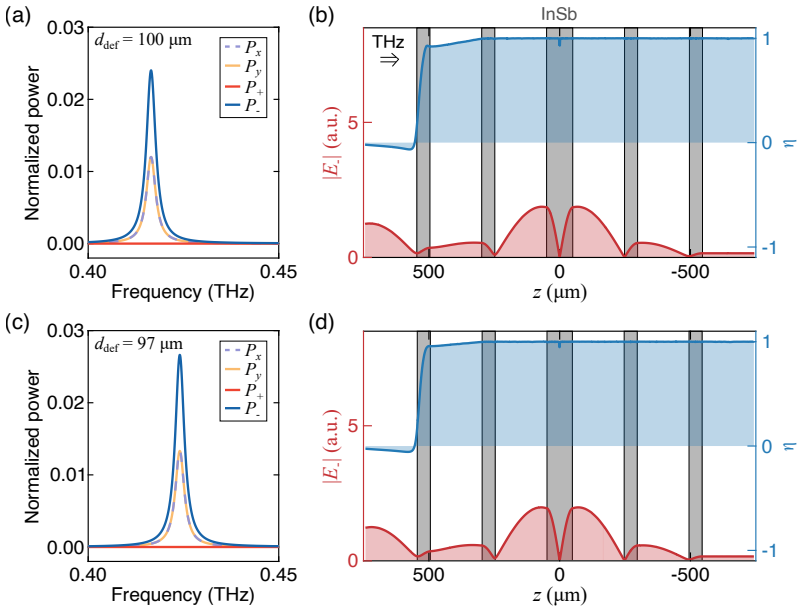

Fig. S1 Transmittance spectra and mode profiles of a chiral 1D-PCC consisting of five InSb layers. The simulation results when the thickness of the layer (iii) is (a)–(b) 100 μm and (c)–(d) 97 μm, respectively.

S3 Magnetic Field Dependence of the Chiral PCC

We examined the properties of the cavity mode of our optimized chiral PCC design at three different magnetic fields ($B = 0\,\mathrm{T}$,1 T, and 7 T), as shown in Fig. S3. The structure is Design II: layers (i)–(ii) and (iv)–(v) are InSb whereas layer (iii) is silicon. At $B = 0\,\mathrm{T}$, the PCC is linear since TRS is not broken. Consequently, the transmitted light remains linearly polarized [Fig. S3(a)] and $\eta(z)$ is close to 0 [Fig. S3(b)]. Note that the peak amplitude of $|E_-(z)|$ in the chiral 1D-PCC is lower than that in the linear 1D-PCC due to losses in the magnetoplasma.

At $B = 1\,\mathrm{T}$, the transmittance spectrum for P_x exhibits two peaks, as shown in Fig. S3(c). This is because the peak frequencies differ for the two opposite handedness; the peak frequency of P_- is higher than that of P_+. This feature can be utilized as a filter for circularly polarized light. However, $\eta(z) \neq 1$ at z_{max} [Fig. S3(d)], indicating that the cavity electric field is not fully circularly polarized at this B.

At high B, such as $B = 7\,\mathrm{T}$, ω_{c} in InSb exceeds ω_{cav} significantly. The peaks for P_+ and P_- coalesce [Fig. S3(e)], and $\eta(z_{\mathrm{max}})$ decreases to 0 [Fig. S3(f)]. Therefore, these simulation results show that the chiral 1D-PCC is effective only when ω_{c} and ω_{cav} are approximately equal.

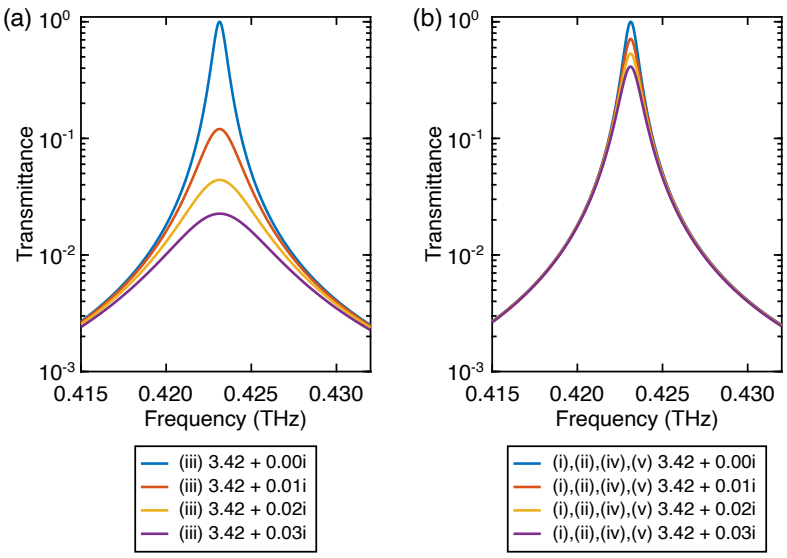

Fig. S2 Effects of losses on transmittance spectra. The transmittance spectra when κ of (a) layer (iii) and (b) layers (i)–(ii) & (iv)–(v) increases, respectively. The spectra were calculated using the TMM.

The properties of the chiral PCC at $B = -0.212\,\mathrm{T}$ are identical to those at $B = 0.212\,\mathrm{T}$, except that the roles of P_- and P_+ are interchanged and $\eta(z = z_{\max}) = -1$, as shown in Fig. S4.

S4 Chiral Tamm cavities

This section studies chiral Tamm cavities. The Tamm cavities consist of three silicon layers with identical thicknesses separated by air. The thicknesses of the silicon and air layers are 50 μm and 198 μm, respectively. The back side of the third silicon layer is coated by a 100 nm gold (Au) layer.

Fig. S5(a) and (b) display reflected power spectra and mode profiles of the Tamm cavity. The incident light is linearly polarized in the x direction. The reflected power spectra show a resonance at 0.4225 THz, and the reflected light is linearly polarized ($P_x \approx 2P_+ = 2P_-, P_y \approx 0$). The electric field is mainly localized at the front side of the third silicon layer.

By replacing the first two silicon layers with InSb, the resonance of the Tamm cavity becomes chiral. The reflected power spectra and mode profiles of a chiral Tamm cavity are shown in Fig. S5(c) and (d). An external magnetic field of $B = 0.212\,\mathrm{T}$ is considered in the calculation. For the chiral Tamm cavity, the reflected power $P_+ > 0$ because the front side of the first wafer reflects light in both circular polarizations. However, the cavity resonance is only observable in the P_- spectrum. The mode profile indicates that the electric field at the maximum position is circularly polarized ($\eta \approx 1$).

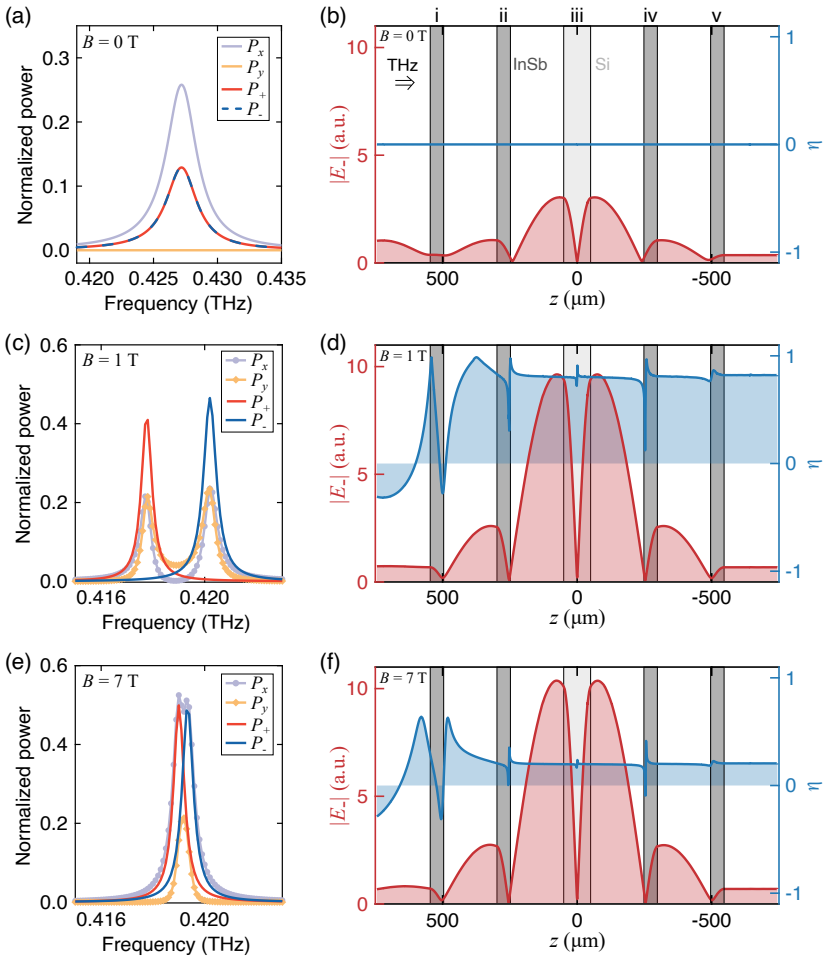

Fig. S3 The properties of the optimized chiral 1D-PCCs (Design II) at different magnetic fields, B. Transmittance spectra and mode profiles of the chiral 1D-PCCs at (a)–(b) $B = 0\,\mathrm{T}$, (c)–(d) $B = 1\,\mathrm{T}$, and (e)–(f) $B = 7\,\mathrm{T}$, respectively. All layers are InSb except layer (iii). The $|E_-(z)|$ and $\eta(z)$ profiles are plotted at the peak frequency of P_-. The incident light is linearly polarized in the x axis.

S5 Calculation of vacuum electric field

The mode profiles of the chiral cavity modes were calculated using COMSOL Multiphysics software. In this case, we assumed that the cavity was excited by a circularly polarized plane wave with an electric field amplitude of 1 V/m. To calculate the variance of the electric field in the vacuum state, $E_{\mathrm{vac},-}$, we normalized the electric field

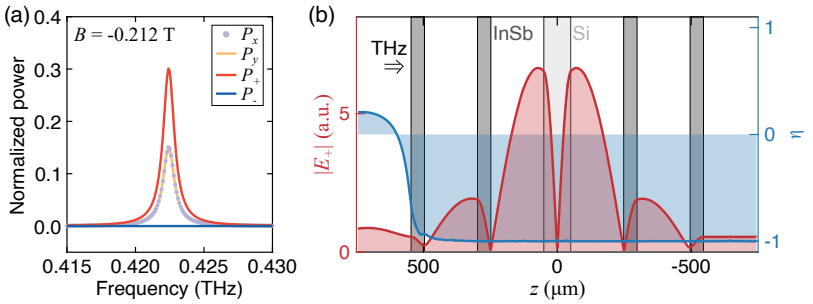

Fig. S4 The properties of the chiral 1D-PCC at negative B. (a) Transmittance spectrum and (b) mode profile of the chiral cavity mode at $B = -0.212\,\mathrm{T}$. The incident light is linearly polarized in the x direction.

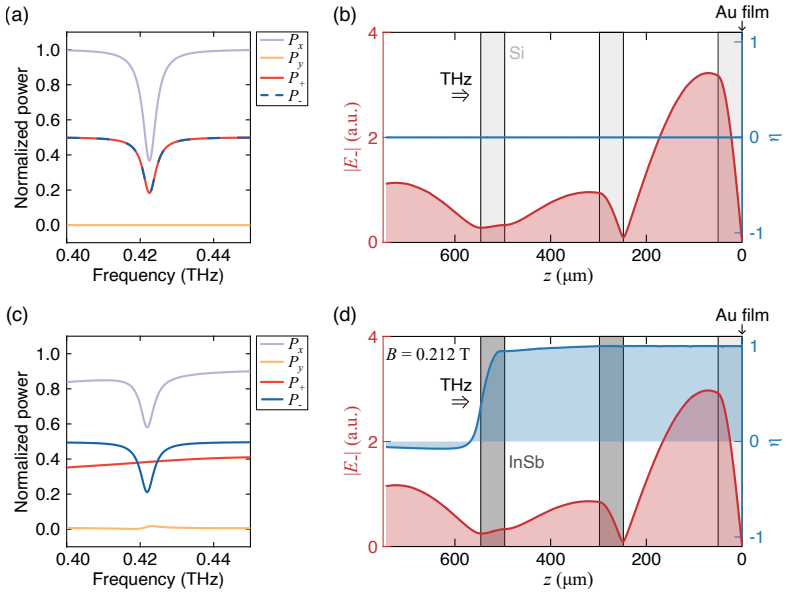

Fig. S5 Transmittance spectra and mode profiles of chiral Tamm cavities. The simulation results for (a)–(b) a linear Tamm cavity and (c)–(d) a chiral Tamm cavity.

extracted from the simulations, $E_{\mathrm{sim},-}$, such that the following relation is satisfied [1, 2]:

$$\int_V dr \varepsilon_0 \varepsilon_r(r) E^2_{\mathrm{vac},-}(r) = \frac{\hbar\omega}{2}, \tag{S1}$$

where ε_r denotes the relative permittivity, $\hbar$ denotes the reduced Planck's constant, and V denotes the cavity volume.

$E_{\text{vac,-}}$ can be expressed as

$$E_{\text{vac,-}}(z) = \sqrt{\frac{\hbar\omega}{2\varepsilon_0 S}} \frac{E_{\text{sim,-}}(z)}{\sqrt{\int_{L_z} dz \varepsilon_r(z) E^2_{\text{sim,-}}(z)}}. \tag{S2}$$

S is the surface area of the cavity and L_z is the effective cavity length spanning from the front side of the first layer to the back side of the last layer.

S6 The derivation of the tight-binding model of graphene

Within a tight-binding model, a solid is considered as a collection of atoms with electrons well localized around the atoms. Thus, it is convenient to write the matter Hamiltonian of the crystal $\mathcal{H}_{\text{m}}$ as a sum of a Hamiltonian describing an atom $\mathcal{H}_{\text{at}}$ and the potential $\delta V(\mathbf{r})$ describing the rest of the crystal, $\mathcal{H}_{\text{m}} = \mathcal{H}_{\text{at}} + \delta V(\mathbf{r})$. We note that V_{at} and $\delta V(\mathbf{r})$ together give the crystal potential, $V_{\text{crys}}(\mathbf{r}) = V_{\text{at}}(\mathbf{r}) + \delta V(\mathbf{r})$. It is important to mention that for the construction of the tight-binding ansatz,

$$\Psi_{\mathbf{k}}(\mathbf{r}) = a_{\mathbf{k}}\Psi^A_{\mathbf{k}}(\mathbf{r}) + b_{\mathbf{k}}\Psi^B_{\mathbf{k}}(\mathbf{r}) = \sum_{\mathbf{j}} e^{i\mathbf{k}\cdot\mathbf{R_j}} \left[a_{\mathbf{k}}\phi_A(\mathbf{r}-\mathbf{R_j}) + b_{\mathbf{k}}\phi_B(\mathbf{r}-\mathbf{R}^B_{\mathbf{j}})\right], \tag{S3}$$

the localized states of $\mathcal{H}_{\text{at}}$ are used [3, 4]. Then we have,

$$\mathcal{H}^m_{\mathbf{k}} = \begin{pmatrix} \langle\Psi^A_{\mathbf{k}}|\mathcal{H}_m|\Psi^A_{\mathbf{k}}\rangle & \langle\Psi^A_{\mathbf{k}}|\mathcal{H}_m|\Psi^B_{\mathbf{k}}\rangle \\ \langle\Psi^A_{\mathbf{k}}|\mathcal{H}_m|\Psi^B_{\mathbf{k}}\rangle^* & \langle\Psi^B_{\mathbf{k}}|\mathcal{H}_m|\Psi^B_{\mathbf{k}}\rangle \end{pmatrix} \tag{S4}$$

The diagonal elements $\langle\Psi^B_{\mathbf{k}}|\mathcal{H}_m|\Psi^B_{\mathbf{k}}\rangle$ and $\langle\Psi^A_{\mathbf{k}}|\mathcal{H}_m|\Psi^A_{\mathbf{k}}\rangle$ result in coupling between next-nearest neighbor sites, hence we eliminate them. The off-diagonal elements are computed as,

$$\begin{aligned} \langle\Psi^A_{\mathbf{k}}|\mathcal{H}_m|\Psi^B_{\mathbf{k}}\rangle &= \langle\Psi^A_{\mathbf{k}}|\mathcal{H}_{at}|\Psi^B_{\mathbf{k}}\rangle + \langle\Psi^A_{\mathbf{k}}|\delta V|\Psi^B_{\mathbf{k}}\rangle \\ &= E_A \underbrace{\langle\Psi^A_{\mathbf{k}}|\Psi^B_{\mathbf{k}}\rangle}_{=0} + \sum_{\mathbf{j},\mathbf{q}} e^{i\mathbf{k}\cdot(\mathbf{R_j}-\mathbf{R_q})} \int d^3r \phi^*_A(\mathbf{r}-\mathbf{R_q})\delta V(\mathbf{r})\phi_B(\mathbf{r}-\mathbf{R_j}-\boldsymbol{\delta}_3). \end{aligned} \tag{S5}$$

Next we perform the coordinate shift $\mathbf{r} \to \mathbf{r} + \mathbf{R_q}$ and define $\mathbf{R_f} = \mathbf{R_j} - \mathbf{R_q}$ leading to

$$\langle\Psi^A_{\mathbf{k}}|\mathcal{H}_m|\Psi^B_{\mathbf{k}}\rangle = \sum_{\mathbf{f}} e^{i\mathbf{k}\cdot\mathbf{R_f}} \int d^3r \phi^*_A(\mathbf{r})\delta V(\mathbf{r})\phi_B(\mathbf{r}-\mathbf{R_f}-\boldsymbol{\delta}_3) = \sum_{\mathbf{f}} e^{i\mathbf{k}\cdot\mathbf{R_f}} t(|\mathbf{R_f}+\boldsymbol{\delta}_3|) \tag{S6}$$

where $t(|\mathbf{R_f}+\boldsymbol{\delta}_3|)$ is the tunneling matrix element due to the potential $\delta V(\mathbf{r})$, which depends only on the distance between different lattice points. Since we take into account only the nearest neighbor tunneling with the vectors $\mathbf{f} = (f_1, f_2) = (0,0)$, $\mathbf{f} = (1,0)$ and $\mathbf{f} = (0,1)$ and assume no strain, all tunneling elements have the

same strength $t(|\mathbf{R}_{0,0}+\boldsymbol{\delta}_3|) = t(|\mathbf{R}_{1,0}+\boldsymbol{\delta}_3|) = t(|\mathbf{R}_{0,1}+\boldsymbol{\delta}_3|) \equiv t$ where t can be found by density functional theory (DFT) as $t = 2.8$eV [5]. Hence, we find $\langle\Psi^A_{\mathbf{k}}|\mathcal{H}_m|\Psi^B_{\mathbf{k}}\rangle = t\left[1+e^{i\mathbf{k}\cdot\mathbf{a}_1}+e^{i\mathbf{k}\cdot\mathbf{a}_2}\right] = th(\mathbf{k})$.

S7 The DFT input in the microscopic theory of graphene coupled to enhanced vacuum fluctuations

The calculations of density functional theory (DFT) were performed using Vienna ab-initio Simulation Package [6–8]. The basis set was projector augmented plane waves with energy of 500 eV. The Perdew-Burke-Ernzerhof functional was chosen to deal with the exchange-correlation interaction. Spin and spin-orbit coupling were not included. In the reciprocal space, a k-mesh of 9×9×1 was utilized to sample the momentum. To avoid interlayer interaction from the periodic images, a vacuum space larger than 15 Å was incorporated in the directions vertical to the material plane. The geometric structure was relaxed until the force on each atom is smaller than 0.01 eV/Å.

Here we also provide the derivation between the momentum matrix elements in two different bases, Eq. (17) in the main text. The tight-binding Hamiltonian for graphene expressed above in Sec. 6, $\mathcal{H}^m_{\mathbf{k}}$ in terms of the Pauli matrices take the form $\mathcal{H}^m_{\mathbf{k}} = t(d_1(\mathbf{k})\sigma_1 + d_2(\mathbf{k})\sigma_2)$ with

$$d_1(\mathbf{k}) = \cos(\mathbf{k}\cdot\boldsymbol{a}_1)+\cos(\mathbf{k}\cdot\boldsymbol{a}_2)+1, \tag{S7}$$

$$d_2(\mathbf{k}) = \sin(\mathbf{k}\cdot\boldsymbol{a}_1)+\sin(\mathbf{k}\cdot\boldsymbol{a}_2), \tag{S8}$$

where $\boldsymbol{a}_1$ and $\boldsymbol{a}_2$ are the translation vectors $\boldsymbol{a}_1 = \boldsymbol{\delta}_1 - \boldsymbol{\delta_3} = \frac{a}{2}(3,\sqrt{3})$ and $\boldsymbol{a}_2 = \boldsymbol{\delta}_2 - \boldsymbol{\delta_3} = \frac{a}{2}(3,-\sqrt{3})$. It is standard to diagonalize this Hamiltonian: the valence and conduction band energies are $\epsilon_c(\mathbf{k}) = -\epsilon_v(\mathbf{k}) = t\sqrt{d_1^2(\mathbf{k})+d_2^2(\mathbf{k})} = td(\mathbf{k})$, and the states read in terms of sublattice A and B

$$|\Psi^c_{\mathbf{k}}\rangle = \frac{1}{\sqrt{2}}\left(|\Psi^A_{\mathbf{k}}\rangle + \frac{d_1(\mathbf{k})-id_2(\mathbf{k})}{d}|\Psi^B_{\mathbf{k}}\rangle\right), \tag{S9}$$

$$|\Psi^v_{\mathbf{k}}\rangle = \frac{1}{\sqrt{2}}\left(-|\Psi^A_{\mathbf{k}}\rangle + \frac{d_1(\mathbf{k})-id_2(\mathbf{k})}{d}|\Psi^B_{\mathbf{k}}\rangle\right). \tag{S10}$$

Hence the inverse relation is,

$$|\Psi^A_{\mathbf{k}}\rangle = \frac{\sqrt{2}}{2}\left(-|\Psi^v_{\mathbf{k}}\rangle + |\Psi^c_{\mathbf{k}}\rangle\right), \tag{S11}$$

$$|\Psi^B_{\mathbf{k}}\rangle = \frac{\sqrt{2}}{2}\frac{d_1(\mathbf{k})+id_2(\mathbf{k})}{d}\left(|\Psi^v_{\mathbf{k}}\rangle + |\Psi^c_{\mathbf{k}}\rangle\right) \tag{S12}$$

The minimal coupling Hamiltonian for graphene given in the main text requires us to compute $\mathrm{i}\hbar \langle \Psi^A_{\mathbf{k}} | \nabla | \Psi^B_{\mathbf{k}} \rangle$.

$$\langle \Psi^A_{\mathbf{k}} | \nabla | \Psi^B_{\mathbf{k}} \rangle = \frac{\sqrt{2}}{2} \frac{d_1(\mathbf{k}) + i d_2(\mathbf{k})}{d(\mathbf{k})} \Big(- \langle \Psi^v_{\mathbf{k}} | \nabla | \Psi^v_{\mathbf{k}} \rangle + \langle \Psi^c_{\mathbf{k}} | \nabla | \Psi^c_{\mathbf{k}} \rangle - \langle \Psi^v_{\mathbf{k}} | \nabla | \Psi^c_{\mathbf{k}} \rangle + \langle \Psi^c_{\mathbf{k}} | \nabla | \Psi^v_{\mathbf{k}} \rangle \Big). \tag{S13}$$

The diagonal terms can be obtained analytically,

$$\langle \Psi^c_{\mathbf{k}} | \nabla | \Psi^c_{\mathbf{k}} \rangle = \frac{1}{2} \left(\langle \Psi^A_{\mathbf{k}} | + \frac{d_1(\mathbf{k}) + i d_2(\mathbf{k})}{d(\mathbf{k})} \langle \Psi^B_{\mathbf{k}} | \right) \nabla \left(| \Psi^A_{\mathbf{k}} \rangle + \frac{d_1 - i d_2}{d} | \Psi^B_{\mathbf{k}} \rangle \right), \tag{S14}$$

$$\langle \Psi^v_{\mathbf{k}} | \nabla | \Psi^v_{\mathbf{k}} \rangle = \frac{1}{2} \left(- \langle \Psi^A_{\mathbf{k}} | + \frac{d_1(\mathbf{k}) + i d_2(\mathbf{k})}{d(\mathbf{k})} \langle \Psi^B_{\mathbf{k}} | \right) \nabla \left(- | \Psi^A_{\mathbf{k}} \rangle + \frac{d_1(\mathbf{k}) - i d_2(\mathbf{k})}{d(\mathbf{k})} | \Psi^B_{\mathbf{k}} \rangle \right).$$

We already assumed in the microscopic theory $\langle \Psi^A_{\mathbf{k}} | \nabla | \Psi^A_{\mathbf{k}} \rangle = \langle \Psi^B_{\mathbf{k}} | \nabla | \Psi^B_{\mathbf{k}} \rangle = 0$. Hence,

$$\langle \Psi^c_{\mathbf{k}} | \nabla | \Psi^c_{\mathbf{k}} \rangle = \frac{1}{2} \left(\frac{d_1(\mathbf{k}) - i d_2(\mathbf{k})}{d(\mathbf{k})} \langle \Psi^A_{\mathbf{k}} | \nabla | \Psi^B_{\mathbf{k}} \rangle + \frac{d_1(\mathbf{k}) + i d_2(\mathbf{k})}{d(\mathbf{k})} \langle \Psi^B_{\mathbf{k}} | \nabla | \Psi^A_{\mathbf{k}} \rangle \right) \tag{S15}$$

$$\langle \Psi^v_{\mathbf{k}} | \nabla | \Psi^v_{\mathbf{k}} \rangle = -\frac{1}{2} \left(\frac{d_1(\mathbf{k}) - i d_2(\mathbf{k})}{d(\mathbf{k})} \langle \Psi^A_{\mathbf{k}} | \nabla | \Psi^B_{\mathbf{k}} \rangle + \frac{d_1(\mathbf{k}) + i d_2(\mathbf{k})}{d(\mathbf{k})} \langle \Psi^B_{\mathbf{k}} | \nabla | \Psi^A_{\mathbf{k}} \rangle \right).$$

Substituting (S15) in (S13), we obtain

$$\left(1 - \frac{\sqrt{2}}{2}\right) \langle \Psi^A_{\mathbf{k}} | \nabla | \Psi^B_{\mathbf{k}} \rangle = \frac{\sqrt{2}}{2} \left(\frac{d_1(\mathbf{k}) + i d_2(\mathbf{k})}{d(\mathbf{k})} \right)^2 \langle \Psi^B_{\mathbf{k}} | \nabla | \Psi^A_{\mathbf{k}} \rangle - \mathrm{i}\sqrt{2} \frac{d_1(\mathbf{k}) + i d_2(\mathbf{k})}{d(\mathbf{k})} \mathrm{Im} \langle \Psi^v_{\mathbf{k}} | \nabla | \Psi^c_{\mathbf{k}} \rangle. \tag{S16}$$

Also note

$$\left(1 - \frac{\sqrt{2}}{2}\right) \langle \Psi^B_{\mathbf{k}} | \nabla | \Psi^A_{\mathbf{k}} \rangle = \frac{\sqrt{2}}{2} \left(\frac{d_1(\mathbf{k}) - i d_2(\mathbf{k})}{d(\mathbf{k})} \right)^2 \langle \Psi^A_{\mathbf{k}} | \nabla | \Psi^B_{\mathbf{k}} \rangle + \mathrm{i}\sqrt{2} \frac{d_1(\mathbf{k}) - i d_2(\mathbf{k})}{d(\mathbf{k})} \mathrm{Im} \langle \Psi^v_{\mathbf{k}} | \nabla | \Psi^c_{\mathbf{k}} \rangle. \tag{S17}$$

Solving these two equations, we find

$$\langle \Psi^A_{\mathbf{k}} | \nabla | \Psi^B_{\mathbf{k}} \rangle = -\mathrm{i}\sqrt{2} \frac{d_1(\mathbf{k}) + i d_2(\mathbf{k})}{d(\mathbf{k})} \mathrm{Im} \langle \Psi^v_{\mathbf{k}} | \nabla | \Psi^c_{\mathbf{k}} \rangle. \tag{S18}$$

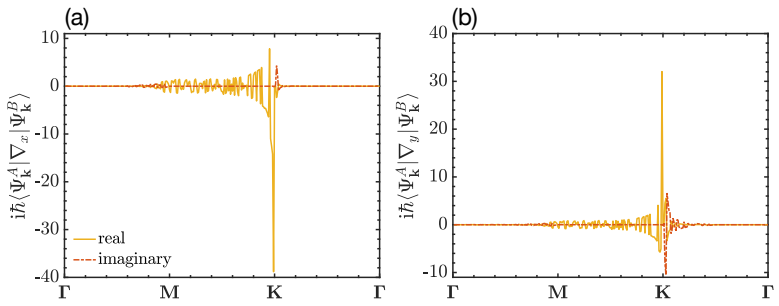

Fig. S6 The matrix elements $\mathrm{i}\hbar\langle\Psi^A_{\mathbf{k}}|\nabla|\Psi^B_{\mathbf{k}}\rangle$ in atomic units computed with Density Functional Theory and the tight-binding model of graphene in x-direction (a) and y-direction (b) with respect to Brillouin zone momenta.

Going back to the momentum units,

$$\mathrm{i}\hbar\langle\Psi^A_{\mathbf{k}}|\nabla|\Psi^B_{\mathbf{k}}\rangle = -\sqrt{2}\frac{d_1(\mathbf{k})+id_2(\mathbf{k})}{d(\mathbf{k})}\mathrm{Re}\left[\mathrm{i}\hbar\langle\Psi^v_{\mathbf{k}}|\nabla|\Psi^c_{\mathbf{k}}\rangle\right]. \tag{S19}$$

We plot $\mathrm{i}\hbar\langle\Psi^A_{\mathbf{k}}|\nabla|\Psi^B_{\mathbf{k}}\rangle$ in atomic units in Figure S6. We observe more than an order of amplitude enhancement in $\mathrm{i}\hbar\langle\Psi^A_{\mathbf{k}}|\nabla|\Psi^B_{\mathbf{k}}\rangle$ at the Dirac node compared to the rest of the Brillouin zone. Since $\mathrm{i}\hbar\langle\Psi^A_{\mathbf{k}}|\nabla|\Psi^B_{\mathbf{k}}\rangle$ dictates the light–matter interaction, such enhancement results in a sizable topological gap.

References

[1] Wang, Z., Gogna, R. & Deng, H. What is the best planar cavity for maximizing coherent exciton-photon coupling. *Appl. Phys. Lett.* **111**, 061102 (2017).

[2] Tay, F. *et al.* Multimode ultrastrong coupling in three-dimensional photonic-crystal cavities (2023). Preprint at arXiv, 2308.12427.

[3] Aschroft, N. W. & Mermin, N. *Solid State Physics* (Harcourt College Publishers, 1976).

[4] Bena, C. & Montambaux, G. Remarks on the tight-binding model of graphene. *New J. Phys.* **11**, 095003 (2009).

[5] Castro Neto, A. H., Guinea, F., Peres, N. M. R., Novoselov, K. S. & Geim, A. K. The electronic properties of graphene. *Rev. Mod. Phys.* **81**, 109–162 (2009).

[6] Kresse, G. & Hafner, J. Ab initio molecular dynamics for liquid metals. *Phys. Rev. B* **47**, 558–561 (1993).

[7] Kresse, G. & Furthmüller, J. Efficiency of ab-initio total energy calculations for metals and semiconductors using a plane-wave basis set. *Comput. Mater. Sci.* **6**, 15–50 (1996).

[8] Kresse, G. & Furthmüller, J. Efficient iterative schemes for ab initio total-energy calculations using a plane-wave basis set. *Phys. Rev. B* **54**, 11169–11186 (1996).